

Search for Gamma Ray Bursts with the ARGO-YBJ Detector in Shower Mode

B. Bartoli^{1,2}, P. Bernardini^{3,4}, X. J. Bi⁵, Z. Cao⁵, S. Catalanotti^{1,2}, S. Z. Chen^{5,*}, T. L. Chen⁶, S. W. Cui⁷, B. Z. Dai⁸, A. D'Amone^{3,4}, Danzengluobu⁶, I. De Mitrì^{3,4}, B. D'Ettorre Piazzoli^{1,9}, T. Di Girolamo^{1,2}, G. Di Sciascio⁹, C. F. Feng¹⁰, Zhaoyang Feng⁵, Zhenyong Feng¹¹, W. Gao⁵, Q. B. Gou⁵, Y. Q. Guo⁵, H. H. He⁵, Haibing Hu⁶, Hongbo Hu⁵, M. Iacovacci^{1,2}, R. Iuppa^{12,13}, H. Y. Jia¹¹, Labaciren⁶, H. J. Li⁶, C. Liu⁵, J. Liu⁸, M. Y. Liu⁶, H. Lu⁵, L. L. Ma⁵, X. H. Ma⁵, G. Mancarella^{3,4}, S. M. Mari^{14,15}, G. Marsella^{3,4}, S. Mastroianni², P. Montini¹⁶, C. C. Ning⁶, L. Perrone^{3,4}, P. Pistilli^{14,15}, P. Salvini¹⁷, R. Santonico^{9,18}, P. R. Shen⁵, X. D. Sheng⁵, F. Shi⁵, A. Surdo⁴, Y. H. Tan⁵, P. Vallania^{19,20}, S. Vermetto^{19,20}, C. Vigorito^{20,21}, H. Wang⁵, C. Y. Wu⁵, H. R. Wu⁵, L. Xue¹⁰, Q. Y. Yang⁸, X. C. Yang⁸, Z. G. Yao⁵, A. F. Yuan⁶, M. Zha⁵, H. M. Zhang⁵, L. Zhang⁸, X. Y. Zhang¹⁰, Y. Zhang⁵, J. Zhao⁵, Zhaxiciren⁶, Zhaxisangzhu⁶, X. X. Zhou^{11,*}, F. R. Zhu¹¹, and Q. Q. Zhu⁵ (The ARGO-YBJ Collaboration)

¹ Dipartimento di Fisica dell'Università di Napoli "Federico II," Complesso Universitario di Monte Sant'Angelo, via Cinthia, I-80126 Napoli, Italy

² Istituto Nazionale di Fisica Nucleare, Sezione di Napoli, Complesso Universitario di Monte Sant'Angelo, via Cinthia, I-80126 Napoli, Italy

³ Dipartimento Matematica e Fisica "Ennio De Giorgi," Università del Salento, via per Arnesano, I-73100 Lecce, Italy

⁴ Istituto Nazionale di Fisica Nucleare, Sezione di Lecce, via per Arnesano, I-73100 Lecce, Italy

⁵ Key Laboratory of Particle Astrophysics, Institute of High Energy Physics, Chinese Academy of Sciences, P.O. Box 918, 100049 Beijing, China

⁶ Tibet University, 850000 Lhasa, Xizang, China

⁷ Hebei Normal University, 050024 Shijiazhuang Hebei, China

⁸ Yunnan University, 2 North Cuihu Road, 650091 Kunming, Yunnan, China

⁹ Istituto Nazionale di Fisica Nucleare, Sezione di Roma Tor Vergata, via della Ricerca Scientifica 1, I-00133 Roma, Italy

¹⁰ Shandong University, 250100 Jinan, Shandong, China

¹¹ Southwest Jiaotong University, 610031 Chengdu, Sichuan, China

¹² Dipartimento di Fisica dell'Università di Trento, via Sommarive 14, 38123 Povo, Italy.

¹³ Trento Institute for Fundamental Physics and Applications, via Sommarive 14, 38123 Povo, Italy

¹⁴ Dipartimento di Fisica dell'Università "Roma Tre," via della Vasca Navale 84, I-00146 Roma, Italy

¹⁵ Istituto Nazionale di Fisica Nucleare, Sezione di Roma Tre, via della Vasca Navale 84, I-00146 Roma, Italy

¹⁶ Dipartimento di Fisica dell'Università di Roma "La Sapienza" and INFN – Sezione di Roma, piazzale Aldo Moro 2, 00185 Roma, Italy

¹⁷ Istituto Nazionale di Fisica Nucleare, Sezione di Pavia, via Bassi 6, I-27100 Pavia, Italy

¹⁸ Dipartimento di Fisica dell'Università di Roma "Tor Vergata," via della Ricerca Scientifica 1, I-00133 Roma, Italy

¹⁹ Osservatorio Astrofisico di Torino dell'Istituto Nazionale di Astrofisica, via P. Giuria 1, I-10125 Torino, Italy

²⁰ Istituto Nazionale di Fisica Nucleare, Sezione di Torino, via P. Giuria 1, I-10125 Torino, Italy

²¹ Dipartimento di Fisica dell'Università di Torino, via P. Giuria 1, I-10125 Torino, Italy

Abstract: The ARGO-YBJ detector, located at the Yangbajing Cosmic Ray Laboratory (4300 m a. s. l., Tibet, China), was a "full coverage" air shower array dedicated to gamma ray astronomy and cosmic ray studies. The wide field of view (~ 2 sr) and high duty cycle ($> 86\%$), made ARGO-YBJ suitable to search for short and unexpected gamma ray emissions like gamma ray bursts (GRBs). Between 2007 November 6 and 2013 February 7, 156 satellite-triggered GRBs (24 of them with known redshift) occurred within the ARGO-YBJ field of view (zenith angle $\theta \leq 45^\circ$). A search for possible emission associated to these GRBs has been made in the two energy ranges 10-100 GeV and 10-1000 GeV. No significant excess has been found in time coincidence with the satellite detections nor in a time window of one hour after the bursts. Taking into account the EBL absorption, upper limits to the energy fluence at 99% of confidence level have been evaluated, with values ranging from $\sim 10^{-5}$ erg cm⁻² to $\sim 10^{-1}$ erg cm⁻².

* Corresponding author: zhouxx@swjtu.edu.cn (X. X. Zhou); chensz@ihep.ac.cn (S. Z. Chen)

Keywords: Gamma ray bursts; Cosmic rays; ARGO-YBJ; Extensive air showers

PACS: 98.70.Rz; 96.40.Pq; 98.70.Sa

1. Introduction

Gamma ray bursts (GRBs) are the brightest explosion of gamma rays observed so far, occurring at unpredictable times and random directions in the sky. After almost 50 years since their discovery (Klebesadel et al. 1973), GRBs are still one of the most enigmatic astrophysical phenomena. Up to now over 6000 GRBs with gamma rays of energies from keV to MeV have been observed by dedicated satellites as CGRO-BATSE, Beppo SAX, HETE-2, Swift and Fermi-GBM. The results of BATSE (on board the CGRO) showed that the arrival directions of GRBs are highly isotropic, favoring a cosmological origin (Meegan et al. 1992). Thanks to the launch of Beppo SAX, that provided a precise localization of several GRBs, the first redshifts could be measured, proving that GRBs sources are cosmological objects (Metzger et al. 1997). Now more than 470 redshifts have been measured, ranging from $z = 0.0085$ for GRB980425^a to the surprising value of $z = 8.1$ for GRB090423 (Salvaterra et al. 2009). These data confirm that most GRBs indeed originate at cosmological distances and hence are likely the most energetic phenomena ever occurred since the Big Bang.

The time duration of GRBs usually ranges from a few seconds to tens of seconds, but occasionally can be as long as a few tens of minutes or as short as a few milliseconds. According to the T_{90} parameter, defined as the time interval in which 90% (from 5% to 95%) of the GRB photons is released, GRBs are usually classified into long ($T_{90} > 2$ s) and short ($T_{90} \leq 2$ s) bursts (Kouveliotou et al. 1993). Short GRBs are mostly associated to mergers of compact objects while long GRBs are related to collapsars (Rosswog et al. 2003; Bloom et al. 2006; Campana et al. 2006; Larsson et al. 2015; Zhang et al. 2016).

The GRBs photons detected by satellite instruments are mostly in the keV-MeV energy range. Thanks to EGRET (on board the CGRO) and LAT (on board Fermi), both designed to detect photons in the MeV-GeV energy range, 74 GRBs (up to the time of writing, 2017 March 20) have been observed to contain photons of energy above 1 GeV, and for 20 of them photons of energy above 10 GeV have been detected (Hurley et al. 1994; Fermi-LAT GRBs Web site^b). In particular Fermi-LAT announced the detection of a 95 GeV photon in coincidence with GRB130427A (Ackermann et al. 2014), the highest energy observed so far from a burst. From these observations we know that at least

^a <http://www.mpe.mpg.de/~jcg/grb980425.html>

^b http://fermi.gsfc.nasa.gov/ssc/observations/types/grbs/lat_grbs

a fraction of GRBs has a high energy tail, reaching 1-10 GeV or even more. At the same time, some theoretical models also predict the emission of high energy photons from GRBs (Ma et al. 2003; Beloborodov et al. 2014; Hascoet et al. 2015).

Though much progress has been achieved from satellite-based experiments and theoretical efforts, lots of basic questions still remain unresolved (Ackermann et al. 2014). Which are the energy source and the acceleration mechanism of GRBs? Is there any GRB originating in our Galaxy? In order to understand the whole process picture, it is important to improve the sample of GRBs with high energy emission and to measure the multi-wavelength energy spectrum. Furthermore, since the flux of high energy photons should be strongly attenuated by the interaction with the extragalactic background light (EBL), the detection of photons with energy above 10 GeV from high redshift sources could be of extreme importance in constraining the EBL theoretical models.

Due to the limited size of the space detectors and the rapid fall of GRB energy spectra, satellite-based experiments hardly cover the energy region $E > 10\text{-}100$ GeV. Ground-based experiments, including imaging atmospheric Cherenkov telescopes (IACTs) and extensive air shower (EAS) arrays, can easily reach much larger effective areas, and can be used for the detection of the GRBs high energy component. Searches for GeV-TeV emission from GRBs have been done by many ground-based experiments, such as MAGIC (Albert et al. 2006; Aleksić et al. 2014), HESS (Abramowski et al. 2014), VERITAS (Acciari et al. 2011), Milagro (Atkins et al. 2000 & 2005; Abdo et al. 2007), GRAND (Poirier et al. 2003), HEGRA (Padilla et al. 1998), HAWC (Abeysekara et al. 2015), EAS-TOP (Aglietta et al. 1996), INCA (Castellina et al. 2001), Tibet AS γ (Amenomori et al. 1996; Ding et al. 1997; Zhou et al. 2009) and IceCube (Aartsen et al. 2016). However, no significant events have been observed so far, although some positive indications have been reported. The science prospects for GRBs with CTA have been provided by Inoue et al. (2013). The EAS array LHAASO is currently under construction in Sichuan, China, at 4410 m a. s. l. and will begin to take data with a partial array in 2018. The prospects for GRB detection with LHAASO has been discussed by Chen et al. (2015).

Besides a wide field of view and a high duty cycle (fundamental detector properties for the observation of unpredictable and short duration events as GRBs), ARGO-YBJ has two additional key features: the high altitude and the full coverage, making possible the detection of very small showers generated by gamma rays of energy well below 1 TeV. This capability is essential for the GRBs detection, since photons of higher energy originated at cosmological distances are mostly absorbed in the extragalactic space due to pair production with the UV, optical and infrared photons of EBL.

The GRB search by ARGO-YBJ can be done with two different techniques: scaler mode (Vernetto 2000) and shower mode. In scaler mode the data are the single particle counting rate of the detector. A burst candidate would appear as an excess of counts in coincidence with a satellite GRB with no information about the GRB direction. In shower mode, the events are reconstructed and their arrival direction and energy are measured with an offline process, and a burst candidate would appear as a cluster of showers with arrival direction consistent with that of the satellite GRB. The selection of showers according to their direction significantly decreases the background with respect to the scaler mode. On the other hand, the requirement of a minimum number of particles to trigger the detector increases the primary energy threshold.

The ARGO-YBJ results of a search in scaler mode in coincidence with satellite GRBs have been reported in Aielli et al. (2009a) and in Bartoli et al. (2014a) in the energy range 1-100 GeV. In shower mode, the study of the sensitivity to detect GRBs is given by Zhou et al. (2007, 2016), while the results of a first search for GRBs using the data recorded before 2009 January are reported in Aielli et al. (2009b). The results in shower mode concerning the whole sample of data recorded during the ARGO-YBJ lifetime, from 2007 November 6 to 2013 February 7, will be presented and discussed in this paper.

2. The ARGO-YBJ experiment

The ARGO-YBJ experiment, located at the Yangbajing Cosmic Ray Laboratory in Tibet, China, at an altitude of 4300 m a. s. l., was mainly devoted to gamma ray astronomy (Bartoli et al. 2013, 2014b, 2015a) and cosmic ray physics (Bartoli et al. 2015b, 2015c). The detector is composed of a single layer of resistive plate chambers (RPCs), operated in streamer mode, with a modular configuration. The basic module is a cluster ($5.7 \times 7.6 \text{ m}^2$), composed of 12 RPCs ($1.23 \times 2.85 \text{ m}^2$ each). Each RPC is read out by 10 pads ($55.6 \times 61.8 \text{ cm}^2$ each), representing the space-time pixels of the detector. The clusters are disposed in a central full-coverage carpet (130 clusters on an area $74 \times 78 \text{ m}^2$ with an active area of $\sim 93\%$). In order to improve the performance of the experiment in determining the shower core position, the central carpet is surrounded by 23 additional clusters (“guard ring”). The total area of the array is $110 \times 100 \text{ m}^2$. More details of the detector can be found in Aielli et al. (2006). The installation of the whole detector was completed in the spring of 2007, and the data taking started in 2007 November with a trigger rate of $\sim 3.5 \text{ kHz}$. In 2013 February the detector was definitively switched off.

The ARGO-YBJ detector was connected to two independent data acquisition systems, corresponding to the shower and scaler operation modes. In scaler mode, the total counts of each

cluster are recorded every 0.5 s. In shower mode, the detector is triggered when at least 20 pads in the central carpet are fired within a time of 420 ns. The information on the arrival time and location of each hit are recorded to reconstruct the shower front shape and the arrival direction. These data are used for gamma astronomy studies and to the search of GRBs in shower mode.

3. Data selection and analysis

From 2007 November 6 to 2013 February 7, 188 GRBs occurred in the ARGO-YBJ field of view (zenith angle $\theta \leq 45^\circ$). 99 of them were detected by Fermi (selected from the Fermi GBM Burst Catalog Web site^c) and 89 by Swift and other detectors (selected from Swift and GCN Web sites^d). The present analysis is carried out on 156 of them, since the remaining 32 occurred when the detector was not operating, or the localization by Fermi was too poor (i.e. error boxes larger than 10°).

As GRB photons of energy above ~ 1 TeV (or even below, for very large distances) are likely to be absorbed by the EBL, we assume a GRB power law spectrum with a sharp cutoff at two different maximum energies: 100 GeV and 1 TeV. Since showers generated by photons of energy $E < 10$ GeV cannot trigger the ARGO-YBJ detector, we limit our search to the two energy ranges 10-100 GeV and 10-1000 GeV. The selection of events with these primary energies is done by selecting the showers according to the number of fired pads (N_{pad}). To evaluate the N_{pad} intervals optimized for the two energy ranges considered, we use Monte Carlo simulations: the CORSIKA7.3700 code to describe the development of extensive air showers in the atmosphere, and a code based on GEANT4 (Agostinelli et al. 2003) to simulate the detector response. The corresponding intervals are $N_{\text{pad}} = 20-60$ for $E = 10-100$ GeV and $N_{\text{pad}} = 20-500$ for $E = 10-1000$ GeV (see Table 1).

The effective area A_{eff} of ARGO-YBJ in the two N_{pad} intervals has been calculated for gamma ray energies from 10 to 1000 GeV using the expression:

$$A_{\text{eff}}(E, \theta) = \frac{n_s}{N} \cdot A_s \cdot \cos \theta, \quad (1)$$

where n_s is the number of successfully reconstructed shower events in a given N_{pad} range, N is the total number of events generated by CORSIKA, and A_s is the sampling area ($200 \times 200 \text{ m}^2$). Fig. 1 and 2 show the effective area as a function of the primary energy in the two N_{pad} ranges, for different zenith angles. The effective area for vertical showers with $N_{\text{pad}} = 20-60$ ranges from $\sim 0.01 \text{ m}^2$ at 10 GeV to $\sim 50 \text{ m}^2$ at 100 GeV, while the effective area reaches $\sim 10000 \text{ m}^2$ at 1 TeV using the events with $N_{\text{pad}} =$

^c <http://heasarc.gsfc.nasa.gov/W3Browse/fermi/fermigtrig.html>

^d http://swift.gsfc.nasa.gov/archive/grb_table; http://gcn.gsfc.nasa.gov/gcn3_archive.html

20-500. The effective areas significantly decrease at large zenith angles. At 100 GeV, the effective area for $\theta = 30^\circ$ (40°) is about a factor 6 (50) smaller than for vertical photons.

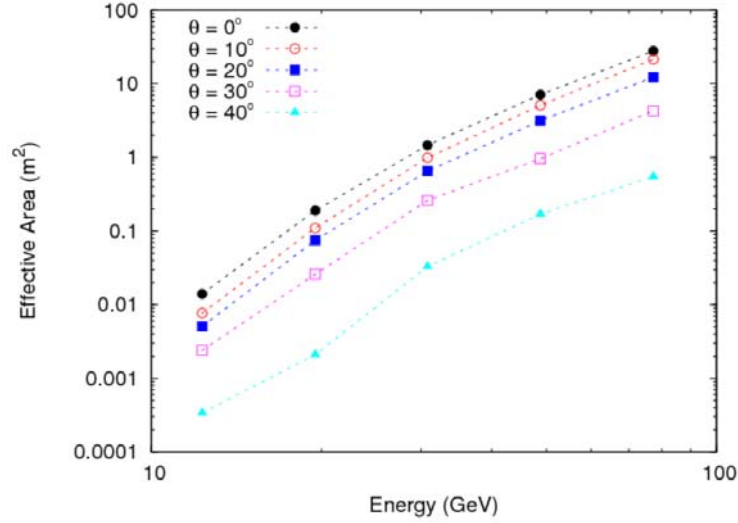


Figure 1. Effective area of ARGO-YBJ for events with $N_{\text{pad}} = 20-60$ and different zenith angles, as a function of the primary energy.

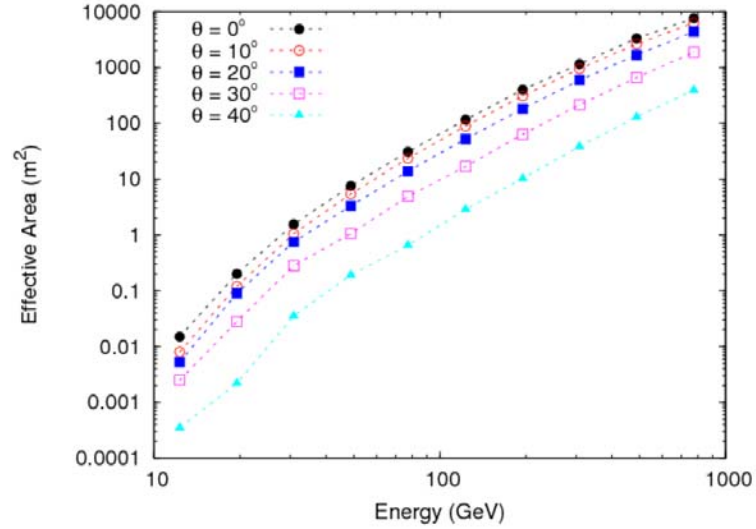


Figure 2. Effective area of ARGO-YBJ for events with $N_{\text{pad}} = 20-500$ and different zenith angles, as a function of the primary energy.

In the ARGO-YBJ data, a GRB would appear as a cluster of showers with arrival directions concentrated in a small sky window, whose size is related to the angular resolution of the detector. In our analysis, the radius of the search window (defined as the “on-source window”) is chosen to maximize the signal to background ratio. According to simulations, the best opening angle radius Ψ_{70} is 3.8° and 2.6° for the two N_{pad} ranges adopted in the analysis, respectively, and contains 71.5% of the signal events.

Table 1

N_{pad} ranges and corresponding angular window radii for gamma rays in two different energy ranges

Energy (GeV)	N_{pad}	Ψ_{70} ($^{\circ}$)
10-100	20-60	3.8
10-1000	20-500	2.6

Due to the different angular resolution to determine the arrival direction of GRBs by different satellite experiments, the position of our on-source window is defined by two approaches. For the 78 GRBs detected by Swift and other satellites excluding Fermi (we call them for simplicity ‘‘Swift GRBs’’ since the large majority of them has been detected by Swift), the position is determined with a precision much better than the angular resolution of ARGO-YBJ. In this case the on-source window is centered at the position reported by the satellite. For 77 of 78 GRBs detected by Fermi-GBM (we call them ‘‘Fermi GRBs’’), the uncertainty in the position is often greater than 1° (Connaughton et al. 2015). In this case our on-source window is shifted inside the Fermi error box, by steps of $\Psi_{70}/2$ in right ascension and declination, to cover the whole region (defined by including statistical and systematic errors). GRB090902B, even if detected by Fermi, has been analyzed as a ‘‘Swift GRB’’ because of the precise localization determined by Swift.

From the observations of satellite instruments (Hurley et al. 1994; Abdo et al. 2009) and some theoretical models (Dermer & Chiang 2000; Pe’er & Waxman 2004), we know that the acceleration mechanism for high-energy gamma rays could be different from that at low energies, and consequently the burst start time and duration could be different from what recorded in the keV-MeV energy range. The Fermi-LAT results and recent models all show that the high energy emissions from GRBs are in the prompt phase or at delayed times (Hascoet et al. 2015). To take into account these possibilities, our search for GRB counterparts is performed in one hour after the GRB satellite trigger time. To investigate possible different durations of the high energy emission, we use the T_{90} given by satellite measurements, and also the time windows $\Delta t = 0.5, 1, 3, 6, 12, 24, 48$ and 96 s, that are shifted by steps of $0.25, 0.5, 1, 2, 3, 6, 12$ and 24 s, respectively, inside the interval of one hour after the GRB start time.

For each trial, defined by time duration, start time and on-source window position, we compare the number of detected events N_{on} with the number of the expected background events due to cosmic rays $\langle N_{\text{b}} \rangle$, and we calculate the chance probability P_{b} of having a number of events equal or larger than N_{on} , and the corresponding statistical significance S in standard deviations (s.d.).

The number of the expected background events $\langle N_b \rangle$ is estimated using the “equi-zenith-angle” method (Zhou 2003), i.e. using the events with the same zenith angle but with different azimuth, detected during two hours around the GRB time. The choice of this time interval comes from the observation that the cosmic ray detection rate (that can fluctuate up to a few percent on time scales of several hours due to atmospheric pressure and temperature variations) in two hours can be considered stable enough for our purposes. Note that due to the atmospheric absorption the background rate is strongly dependent on the zenith angle. As an example, Fig. 3 shows the average background event rate $\langle N_b \rangle$ as a function of the zenith angle, measured during two hours around the time of GRB110705364, for the two angular windows of radius 3.8° and 2.6° .

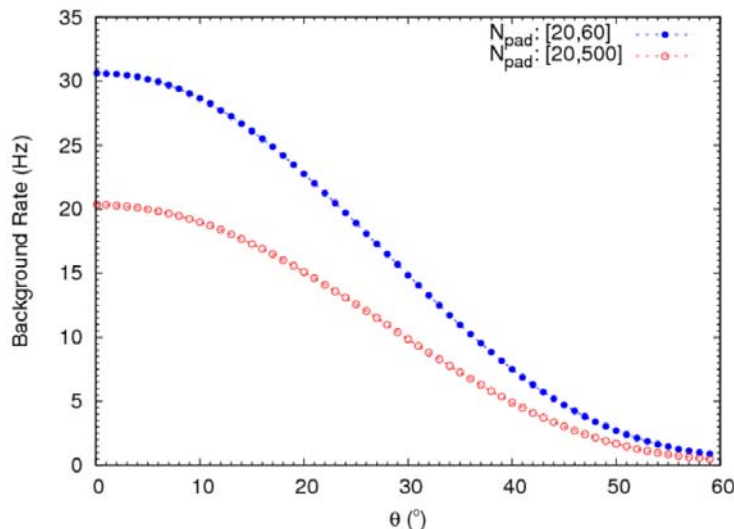


Figure 3. Background event rate as a function of the zenith angle, inside the angular windows used for the analysis in two N_{pad} ranges. The data have been recorded during two hours around the GRB110705364 trigger time.

4. Results

4.1. Analysis of Swift GRBs

The distribution of the chance probability P_b for all the events in coincidence with the 79 Swift GRBs is shown in Fig. 4, while the corresponding significances S are given in Fig. 5. These figures show the results of the analysis in the two N_{pad} ranges previously defined, merged together. The significance distribution is consistent with a Gauss function (solid black line in the figure), showing that the cluster multiplicities are consistent with background fluctuations. It is however interesting to report the details of the most significant clusters.

For the N_{pad} range 20-60, the cluster with the lowest probability is related to GRB080207, whose position (α_o, δ_o) determined by Swift is $(13^{\text{h}}50^{\text{m}}03^{\text{s}}.12, 07^{\circ}31'01'')$. It is delayed by 2502 s, and occurs at a zenith angle of 23.5° . This cluster contains 746 showers in 24 s, while the expected number of background events is 617.96. The corresponding poissonian chance probability is 2.98×10^{-7} , with a

significance of 5.0 s.d.. Taking into account for the number of trials (2.05×10^6), the chance probability is 6.11×10^{-1} (-0.28 s.d.).

For the N_{pad} range 20-500, the lowest probability cluster refers to GRB081025, whose position (α_0 , δ_0) determined by Swift is ($16^{\text{h}}21^{\text{m}}11^{\text{s}}.52$, $60^{\circ}27'58''$). It is delayed by 3186 s, and occurs at a zenith angle of 32.8° . This cluster contains 28 air showers in 1 s, while the expected number of background events is 8.88. The chance probability is 1.53×10^{-7} , corresponding to 5.12 s.d.. After taking into account for the number of trials, the chance probability is 3.13×10^{-1} (0.49 s.d.).

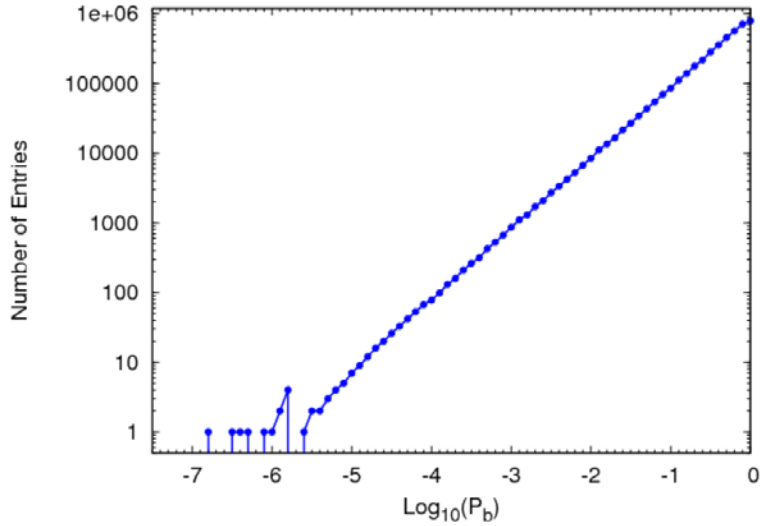


Figure 4. Probability distribution of the 4.1×10^6 clusters in coincidence with 79 Swift GRBs.

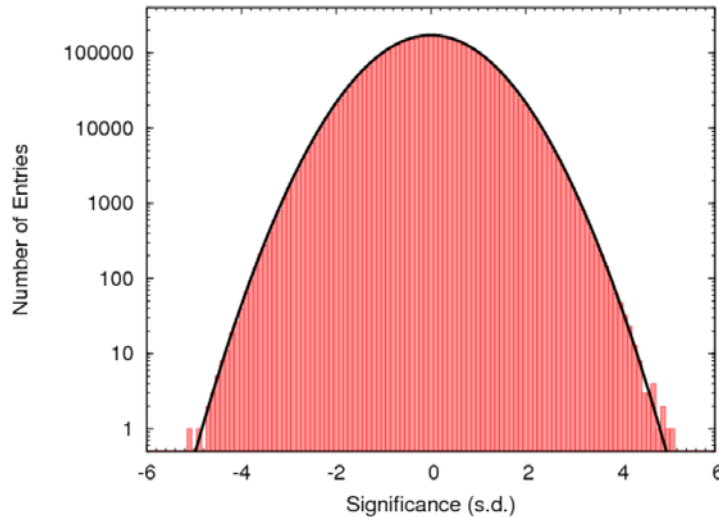


Figure 5. Significance distribution of the 4.1×10^6 clusters in coincidence with 79 Swift GRBs. The solid black line is the normal Gaussian function.

4.2. Analysis of Fermi GRBs

The distribution of the chance probability P_b for all the clusters in coincidence with 77 Fermi GRBs is shown in Fig. 6, while the corresponding significances S are given in Fig. 7. Also in this case the distributions show no statistically significant excess for this sample.

For the N_{pad} range 20-60, the lowest probability cluster is related to GRB081122520, whose position (α_o, δ_o) determined by Fermi is $(22^{\text{h}}36^{\text{m}}24^{\text{s}}, 40^{\circ}00'00'')$ with an angular indetermination of 3.8 degrees. The cluster is centered at $(\alpha, \delta) = (22^{\text{h}}51^{\text{m}}35^{\text{s}}.98, 40^{\circ}00'00'')$, at a zenith angle of 10.0° . It is delayed by 1176 s and contains 855 air showers in 24 s, while the expected number of background events is 693.4. The chance probability is 1.57×10^{-9} , corresponding to a significance of 5.92 s.d.. Taking into account for the number of trials (9.01×10^7), the chance probability becomes 1.41×10^{-1} (1.07 s.d.).

For the N_{pad} range 20-500, the lowest probability cluster is connected to GRB100210101, whose position (α_o, δ_o) determined by Fermi is $(16^{\text{h}}17^{\text{m}}31^{\text{s}}.2, 16^{\circ}04'48'')$ with an uncertainty of 7.1 degrees. The cluster is centered at $(\alpha, \delta) = (16^{\text{h}}07^{\text{m}}07^{\text{s}}.18, 12^{\circ}10'48'')$, at a zenith angle of 32.1° . It is delayed 881 s and contains 64 air showers in 3 s, while the expected number of background events is 27.5. The chance probability is 1.38×10^{-9} , corresponding to a significance of 5.95 s.d.. After taking into account for the number of trials (1.79×10^8), the chance probability is 2.47×10^{-1} (0.68 s.d.).

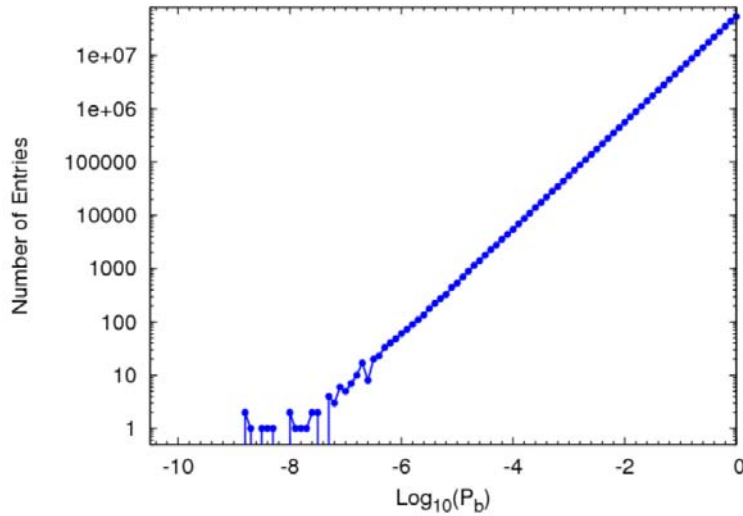


Figure 6. Probability distribution of the 2.69×10^8 clusters in coincidence with 77 Fermi GRBs.

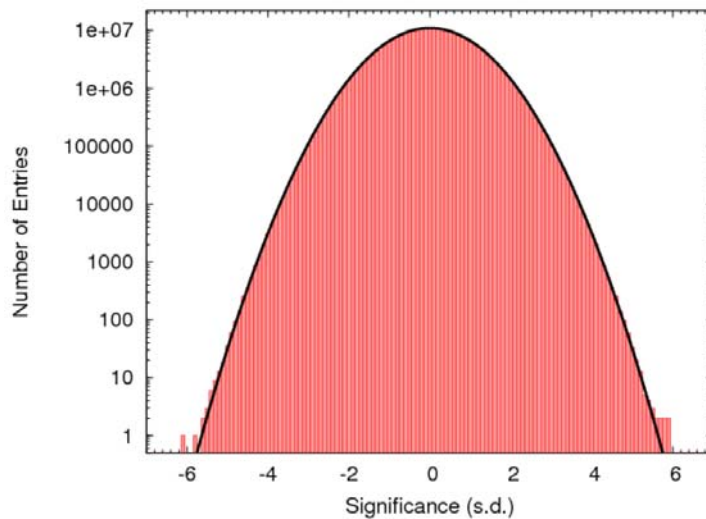


Figure 7. Significance distribution of 2.69×10^8 clusters in coincidence with 77 Fermi GRBs.

The solid black line is the normal Gaussian function.

5. Upper limits to the energy fluence in T_{90}

Since no significant excess has been found in coincidence with 156 satellite-triggered GRBs, we calculate the upper limits to the energy fluence for the two energy ranges considered in the analysis. The fluence upper limits are evaluated during the prompt phase of the emission, i.e. in the time interval T_{90} . Fig. 8 and 9 show the significance distributions of the clusters observed in coincidence with 156 GRBs during T_{90} for two N_{pad} ranges, respectively. For Fermi triggered GRBs, the position of the on-source window is set at the center of the error box. No significance larger than 3 standard deviations is observed.

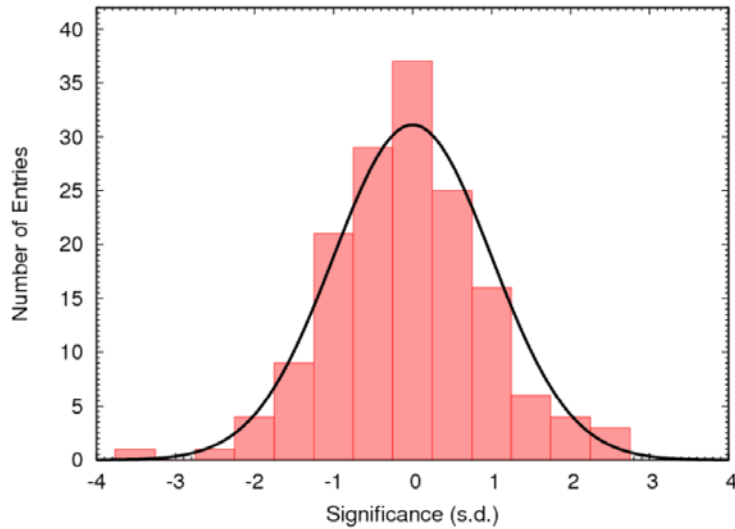


Figure 8. Significance distribution of the clusters detected in coincidence with the prompt phase of 156 GRBs, for the N_{pad} range 20-60. The solid line represents the normal Gauss function.

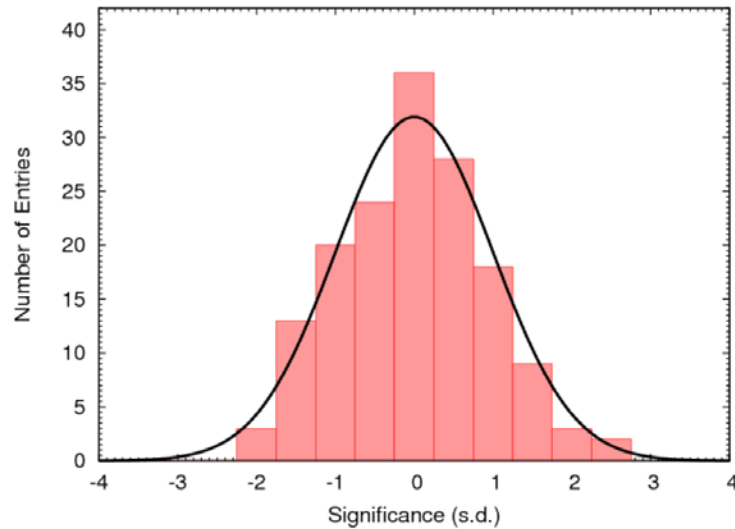


Figure 9. Significance distribution of the clusters detected in coincidence with the prompt phase of 156 GRBs, for the N_{pad} range 20-500. The solid line represents a normal Gauss function.

Given a cluster with a number of detected events N_{on} during the interval T_{90} and an expected number of background events $\langle N_{\text{b}} \rangle$, we calculated the 99% confidence level (C. L.) upper limit on the number of signal events N_{UL} , by using the Feldman-Cousins prescription (Feldman & Cousins 1998). To determine the fluence corresponding to the number of events N_{UL} , we have to make assumptions on the spectral shape of the intrinsic GRB spectrum at high energy and take into account the absorption due to the EBL. According to the observations in the GeV range by CGRO-EGRET (Dingus 2001) and Fermi-LAT (Ackermann et al. 2013), the spectrum has usually a power law shape and the value of the spectral index at high energy is around 2 ($\langle \alpha_{\text{LAT}} \rangle = 2.05 \pm 0.03$ for 35 GRBs see by Fermi-LAT). We assume an intrinsic power law spectrum $dN/dE = KE^{-\alpha}$ with $\alpha = 2.0$, where the normalization K is obtained from the relation:

$$N_{\text{UL}} = K \int_{10 \text{ GeV}}^{E_{\text{cut}}} A_{\text{eff}} \cdot E^{-\alpha} \cdot e^{-\tau_{\text{EBL}}} \cdot dE, \quad (2)$$

Here τ_{EBL} is the optical depth due to the EBL absorption, and E_{cut} is the maximum energy of the spectrum ($E_{\text{cut}} = 100 \text{ GeV}$ or 1 TeV). Concerning the EBL absorption, we use the Gilmore model with a semi-analytical approach (Gilmore et al. 2012), whose parameters at different energies and redshifts can be downloaded from the web site^c. Finally, the upper limit to the fluence F_{UL} is given by:

$$F_{\text{UL}} = K \int_{10 \text{ GeV}}^{E_{\text{cut}}} E \cdot E^{-\alpha} \cdot dE. \quad (3)$$

Note that the redshift was measured for only 24 GRBs of our sample. For the bursts with unknown redshift, we calculate the EBL absorption assuming the mean observed redshift $z = 0.6$ for short GRBs ($T_{90} \leq 2 \text{ s}$) and $z = 2.0$ for long GRBs ($T_{90} > 2 \text{ s}$) (Jakobsson et al. 2006; Berger et al. 2005; Berger 2014).

Table 2 shows information on the 132 GRBs with unknown redshift, together with the calculated fluence upper limits that are in the range $\sim 10^{-5}$ - $10^{-2} \text{ erg cm}^{-2}$ for $E_{\text{cut}} = 100 \text{ GeV}$ and $\sim 10^{-5}$ - $10^{-1} \text{ erg cm}^{-2}$ for $E_{\text{cut}} = 1 \text{ TeV}$.

Fig. 10 and Fig. 11 show the fluence upper limits as a function of the zenith angle for the two energy ranges considered, respectively. The upper limits increase with the zenith angle, due to the showers absorption at larger atmospheric thickness. In both figures it is evident that short GRBs (assumed at $z = 0.6$) have upper limits much smaller than long GRBs (assumed at $z = 2.0$), due to the lower effect of the EBL absorption.

^c <http://physics.ucsc.edu/~joel/EBLdata-Gilmore2012/>

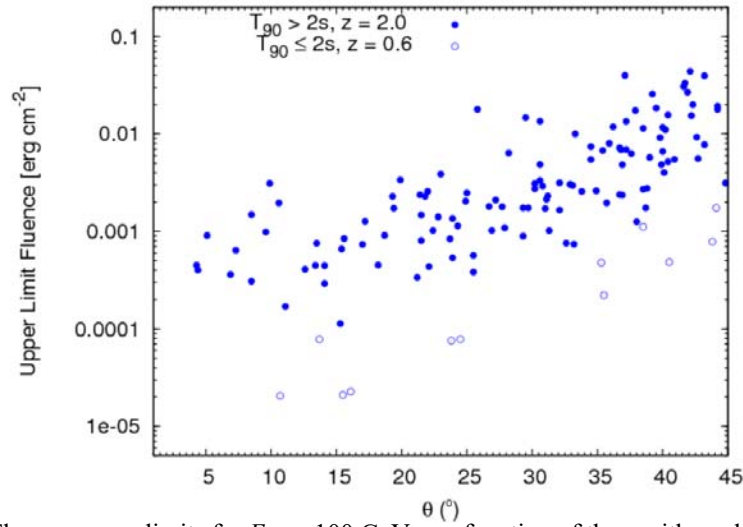


Figure 10. Fluence upper limits for $E_{\text{cut}} = 100$ GeV as a function of the zenith angle. Full dots are for long GRBs, circles for short ones.

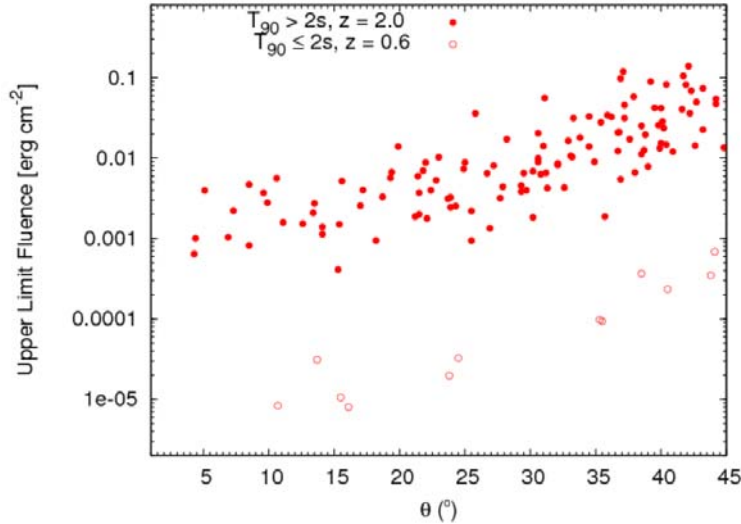


Figure 11. Fluence upper limits for $E_{\text{cut}} = 1$ TeV as a function of the zenith angle. Full dots are for long GRBs, circles for short ones.

For the 24 GRBs with known redshift, a more accurate estimation of the absorption can be done, providing more reliable fluence upper limits, given in Table 3 together with the GRBs data. Also in this case the fluence limits are calculated assuming the spectral slope $\alpha = 2.0$. But for GRB090902B, the spectral slope $\alpha = 1.94$ measured by Fermi-LAT is used.

Fig. 12 shows the F_{UL} values as a function of redshift, for the two energy ranges considered in the analysis. The fluence upper limits increase with redshift, since the flux is more absorbed for far sources. It is interesting to note that, for a given GRB, the fluence for $E_{\text{cut}} = 100$ GeV is higher than that for $E_{\text{cut}} = 1$ TeV when $z < 1$; for $z > 1$ the situation is reversed, due to the large absorption of photons with energy above 100 GeV for $z > 1$.

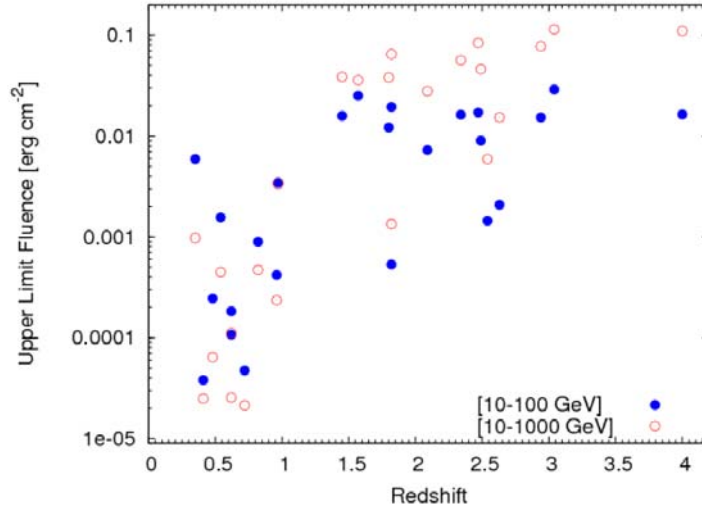


Figure 12. Fluence upper limits as a function of redshift.

Among the GRBs occurred in the ARGO-YBJ field of view, GRB090902B is the Fermi-GBM burst with the highest energy photon (33.4 GeV) detected by Fermi-LAT (Abdo et al. 2009), and for this reason it deserves a special attention. The location was precisely determined by Swift, corresponding to a zenith angle of 23.3° in the ARGO-YBJ field of view. The value of T_{90} is 19.3 s, the redshift 1.82 and the spectral index 1.94. According to our analysis, the clusters observed by ARGO-YBJ at the burst trigger time inside the interval T_{90} for the two N_{pad} ranges (20-60) and (20-500) have a significance of -0.89 and -1.02 s.d., respectively. Since the 33.4 GeV photon was detected 82 seconds after the GBM trigger, i.e. about a minute after the end of the prompt emission, we did a search in coincidence with this delayed GeV emission. We considered 3 time windows: *a*) the interval (0-90 s), including the most energetic photon, *b*) the interval (6-26 s), when the maximum density of GeV photons has been observed, *c*) the interval (82-83 s), i.e. the time around the 33.4 GeV photon. The significance of the clusters detected in the 3 time windows are -1.53, -1.05 and -0.07 s.d., respectively, for $N_{\text{pad}} = 20-60$, and -0.45, -0.41 and 0.74 s.d., respectively, for $N_{\text{pad}} = 20-500$. Using the set of time windows for the standard analysis, the maximum significance is 4.33 s.d. for a time interval of 3 s delayed 2047 s since the burst trigger time. After taking into account for the number of trials, the significance lowers to 0.22 s.d. leading to the conclusion that there are no significant clusters associated to this GRB. Following the method described at the beginning of this section, we evaluated the fluence upper limit in T_{90} at the prompt phase. We found $F_{\text{UL}} = 5.32 \times 10^{-4}$ erg cm $^{-2}$ (1.74×10^{-4} erg cm $^{-2}$ without correction for the EBL absorption) in the energy range 10-100 GeV to be compared with the extrapolated fluence $F_{\text{EX}} = 1.06 \times 10^{-4}$ erg cm $^{-2}$ (obtained by extrapolating up to E_{cut} the flux measured by satellite). In the energy range 10-1000 GeV, we found $F_{\text{UL}} = 1.34 \times 10^{-3}$ erg

cm^{-2} ($4.63 \times 10^{-6} \text{ erg cm}^{-2}$ without correction for EBL absorption) to be compared with $F_{\text{EX}} = 2.28 \times 10^{-4} \text{ erg cm}^{-2}$. Taking into account the EBL absorption, the extrapolated fluences of GRB090902B are lower than the upper limits measured by ARGO-YBJ. According to our calculations, ARGO-YBJ could detect GRB090902B for a redshift lesser than 1.0 and an emission extending up to 1 TeV.

6. Detectability of GRB 130427A

GRB 130427A, detected by both Fermi-GBM and Fermi-LAT, is the burst with the highest energy photons ever observed, reaching 95 GeV. ARGO-YBJ was switched off in 2013 February, two months before the burst, but since the zenith angle of the GRB was greater than 90° , the burst would have been undetectable in any case. It is interesting however to estimate the capability of ARGO-YBJ to detect a burst as bright as GRB 130427A, in case of a more favorable zenith angle.

The measured spectral index of GRB 130427A ranges between $\alpha \sim 2.5$ and $\alpha \sim 1.7$, the total fluence in the 10 keV-100 GeV band is $4.9 \times 10^{-3} \text{ erg cm}^{-2}$ and the duration is $T_{90} = 138.2 \text{ s}$ (Ackermann et al. 2014). Assuming a zenith angle $\theta = 20^\circ$, a spectral index $\alpha = 2.0$, and considering the EBL absorption corresponding to the GRB distance ($z = 0.34$), the estimated minimum fluence detectable by ARGO-YBJ in T_{90} is $1.27 \times 10^{-3} \text{ erg cm}^{-2}$ in the energy range 10-100 GeV, and $2.38 \times 10^{-4} \text{ erg cm}^{-2}$ in the energy range 10-1000 GeV. Assuming a spectrum extending up to 1 TeV with the same spectral index, the fluence of GRB 130427A in the energy range 10-1000 GeV would be $4.7 \times 10^{-4} \text{ erg cm}^{-2}$, twice higher than the ARGO-YBJ sensitivity. Thus, an overhead burst as bright as GRB 130427A and with a photon emission extending up to 1 TeV would have been easily detected by ARGO-YBJ.

7. Conclusions

A search for GeV-TeV burst-like events in coincidence with GRBs detected by satellite was done using the ARGO-YBJ data from 2007 November 6 to 2013 February 7. During more than five years, a total of 156 GRBs was analyzed. After considering the number of trials, the distribution of the chance probabilities for the clusters of events occurred in coincidence with the GRBs (i.e. during T_{90}) or in a time window of one hour after the satellite trigger time is consistent with background fluctuations. None of the examined GRBs, notably the ‘Swift GRBs’, contains high energy ($> 10 \text{ GeV}$) photons with fluxes comparable to that featuring GRB 130427A and spectrum extending up to 1 TeV. Indeed many conditions, as the efficiency of the production mechanism, the source transparency and the attenuation by the EBL, may affect the GeV-TeV fluence .

Since no significant signal has been detected, the 99% C. L. upper limits to the energy fluence

were evaluated. The limits are calculated assuming a power law energy spectrum with spectral index $\alpha = 2.0$ above 10 GeV, a sharp cutoff at the E_{cut} energy (100 GeV or 1 TeV), and taking into account the EBL absorption (assuming a redshift $z = 0.6$ for short GRBs and $z = 2.0$ for long GRBs when the redshift was not available). The obtained fluence upper limits cover a large range of values, depending on the GRB duration, zenith angle and distance, ranging from less than 10^{-5} erg cm $^{-2}$ to 10^{-1} erg cm $^{-2}$.

In the next future, HAWC, CTA and LHAASO (these two currently under construction), given their significantly higher sensitivity, are expected to provide the first measurement of the GeV-TeV emission from gamma ray bursts by ground-based detectors.

Acknowledgements

This work is supported in China by the National Natural Science Foundation of China (NSFC) under the Grant Nos. 11475141, 11575203 and 11375209, the Chinese Ministry of Science and Technology, the Chinese Academy of Sciences (CAS), the Key laboratory of Particle Astrophysics, Institute of High Energy Physics (IHEP), and in Italy by the Istituto Nazionale di Fisica Nucleare (INFN).

References

- Aartsen M. G., Abraham K., Ackermann M., et al. 2016, *ApJ*, **824**, 115
 Abdo A.A., Ackermann M., Ajello M., et al. 2009, *ApJL*, **706**, L138
 Abdo A. A., Allen B. T., Berley D., et al. 2007, *ApJ*, **666**, 361
 Abeysekera A. U., Alfaro R., Alvarez C., et al. 2015, *ApJ*, **800**, 78
 Abramowski A., Aharonian F., Ait Benkhali F., et al. 2014, *A&A*, **565**, A16
 Acciari V. A., Aliu E., Arlen T., et al. 2011, *ApJ*, **743**, 62
 Ackermann M., Ajello M. and Asano K. 2013, *ApJS*, **209**, 11
 Ackermann M., Ajello M., Asano K., et al. 2014, *Science*, **343**, 42
 Agostinelli S., Allison J., Amako K., et al. 2003, *Nucl. Instr. Meth. Phys. Res.*, **A506**, 250
 Aglietta M., Alessandro B., Antonioli P., et al. 1996, *ApJ*, **469**, 305
 Aielli G., Assiro R., Bacci C., et al. 2006, *Nucl. Instrum. Meth.*, **A562**, 92
 Aielli G., Bacci C., Barone F., et al. 2009a, *ApJ*, **699**, 1281
 Aielli G., Bacci C., Bartoli B., et al. 2009b, *Astropart. Phys.*, **32**, 47
 Albert J., Aliu E., Anderhub H., et al. 2006, *ApJL*, **641**, L9
 Aleksić J., Ansoldi S., Antonelli L. A., et al. 2014, *MNRAS*, **437**, 3103
 Amenomori M., Cao Z., Dai B. Z., et al. 1996, *A&A*, **311**, 919
 Atkins R., Benbow W., Berley D., et al. 2000, *ApJ*, **533**, L119
 Atkins R., Benbow W., Berley D., et al. 2005, *ApJ*, **630**, 996
 Bartoli B., Bernardini P., Bi X. J., et al. 2013, *ApJ*, **779**, 27
 Bartoli B., Bernardini P., Bi X. J., et al. 2014a, *ApJ*, **794**, 82
 Bartoli B., Bernardini P., Bi X. J., et al. 2014b, *ApJ*, **790**, 152
 Bartoli B., Bernardini P., Bi X. J., et al. 2015a, *ApJ*, **806**, 20
 Bartoli B., Bernardini P., Bi X. J., et al. 2015b, *Phys. Rev. D*, **92**, 092005
 Bartoli B., Bernardini P., Bi X. J., et al. 2015c, *Phys. Rev. D*, **91**, 112017

- Beloborodov A. M., Hascoët R. and Vurm I., 2014, *APJ*, **788**, 36
- Berger E. 2014, *ARA&A*, **52**, 43
- Berger E., Kulkarni S. R., Fox D. B., et al. 2005, *ApJ*, **634**, 501
- Bloom J. S., Prochaska J. X., Pooley D., et al. 2006, *ApJ*, **638**, 354
- Campana S., Mangano V., Blustin A. J., et al. 2006, *Nature*, **442**, 1008
- Castellina A., Ghia P. L., Kakimoto F., et al., 2001, *Nuovo Cim.*, **C24**, 631
- Chen S. Z., Di Girolamo T., He H. H., et al. 2015, in Proc. 34th ICRC (the Hague, the Netherlands), PoS (ICRC2015) 728
- Connaughton V., Briggs M. S., Goldstein A., et al. 2015, *ApJS*, **216**, 32
- Dermer C. D. and Chiang J. 2000, *AIP Conf. Proc.*, **515**, 225
- Ding L. K., Zhaxiciren, Zhaxisanzhu, et al. 1997, *HEP&NP*, **21**, 673 (in Chinese)
- Dingus B. L. 2001, *AIP Conf. Proc.*, **558**, 383
- Feldman G. J. and Cousins R. D. 1998, *Phys. Rev. D*, **57**, 3873
- Gilmore R. C., Somerville R. S., Primack J. R., et al. 2012, *Mon. Not. R. Astron. Soc.*, **422**, 3189
- Hascoët R., Vurm I. and Beloborodov A. M., 2015, *ApJ*, **813**, 63
- Hurley K., Dingus B. L., Mukherjee R., et al. 1994, *Nature*, **372**, 652
- Inoue S., Granot J., O'BrienInoue P. T., et al. 2013, *Astropart. Phys.*, **43**, 252
- Jakobsson P., Levan A., Fynbo J. P. U., et al. 2006, *A&A*, **447**, 897
- Klebesadel R. W., Strong I. B. and Olson R. A. 1973, *ApJL*, **182**, L85
- Kouveliotou C., Meegan C. A., Fishman G. J., et al. 1993, *ApJL*, **413**, L101
- Larsson J., Racusin J. L. and Burgess J. M. 2015, *ApJ*, **800**, L34
- Ma X. H., Zhou X. X., Wu M., et al. 2003, *HEP&NP*, **27**, 973
- Meegan C. A., Fishman G. J., Wilson R. B., et al. 1992, *Nature*, **355**, 143
- Metzger M. R., Djorgovski S. G., Kulkarni S. R., et al. 1997, *Nature*, **387**, 878
- Padilla L., Funk B., Krawczynski H., et al. 1998, *A & A*, **337**, 43
- Pe'er A. and Waxman E. 2004, *ApJ*, **613**, 448
- Poirier J., D'Andrea C., Fragile P. C., et al. 2003, *Phys. Rev. D*, **67**, 042001
- Rosswog S., Ramirez-Ruiz E. and Davies M. B. 2003, *MNRAS*, **345**, 1077
- Salvaterra R., Valle M. D., Campana S., et al. 2009, *Nature*, **461**, 1258
- Vernetto S. 2000, *Astropart. Phys.*, **13**, 75
- Zhang B., Lü H. J. and Liang E. W., 2016, *Space Sci. Rev.*, **202**, 3
- Zhou X. X. (for the Tibet AS γ collaboration) 2003, in Proc. 28th ICRC (Tsukuba, Japan), pp. 2757-2760
- Zhou X. X., Cheng N., Hu H. B., et al. 2007, *HEP & NP*, **31**, 65
- Zhou X. X., Hu H. B. and Huang Q. 2009, *Acta Phys. Sin.*, **58**, 5879 (in Chinese)
- Zhou X. X., Gao L. L., Zhang Y., et al. 2016, *Chinese Phys. C*, **40**, 075001

Table 2

List on 132 GRBs with unknown redshift occurred in the field of view of ARGO-YBJ

GRB (1)	Satellite (2)	T_{90} (s) (3)	θ ($^\circ$) (4)	keV fluence (10^{-7} erg cm^{-2}) (keV range) (5)	σ_1 (10-100 GeV) (6)	σ_2 (10-1000 GeV) (7)	F_{UL1} (erg cm^{-2}) (10-100 GeV) (8)	F_{UL2} (erg cm^{-2}) (10-1000 GeV) (9)
080328	Swift	90.6	37.2	94 (15-150)	-0.04	-1.69	1.35E-2	4.56E-2
080515	Swift	21	43.2	20 (15-150)	-0.59	-0.41	7.77E-3	2.26E-2
080613B	Swift	105	39.2	58 (15-150)	0.89	1.32	2.57E-2	8.94E-2
080714086	Fermi	5.4	24.3	6.8 (10-1000)	1.82	0.71	1.14E-3	2.53E-3
080726	AGILE	12	36.7	...	1.50	1.03	7.20E-3	2.09E-2
080727C	Swift	79.7	34.5	52 (15-150)	-0.79	0.80	5.46E-3	3.29E-2
080730520	Fermi	17.4	31.2	48.7 (10-1000)	0.03	-0.20	2.31E-3	6.54E-3
080802386	Fermi	0.6	23.8	3.98 (10-1000)	-0.01	-0.70	7.57E-5	1.97E-5
080822B	Swift	64	40.4	1.7 (15-150)	-1.11	-2.00	1.57E-2	8.21E-2
080830368	Fermi	40.9	35.9	70 (10-1000)	0.41	1.36	7.99E-3	3.41E-2
080903	Swift	66	21.4	14 (15-150)	0.94	0.30	2.37E-3	5.94E-3
081025	Swift	23	30.6	19 (15-150)	0.84	0.69	3.33E-3	9.91E-3
081102365	Fermi	1.7	35.3	10.9 (10-1000)	-0.21	-1.01	4.77E-4	9.76E-5
081105	IPN	10	36.7	...	-0.90	-1.06	2.39E-3	1.22E-2
081122520	Fermi	23.3	9.9	75.4 (10-1000)	0.78	1.35	3.11E-3	2.79E-3
081130629	Fermi	45.6	37.9	32.2 (10-1000)	1.82	1.85	1.74E-2	5.80E-2
081215784	Fermi	5.6	31.3	547 (10-1000)	-0.56	0.09	1.02E-3	4.24E-3
081226156	Fermi	65.8	42.7	39.5 (10-1000)	-1.32	0.29	5.60E-3	4.97E-2
090107A	Swift	12.2	40.1	2.3 (15-150)	-0.99	-1.17	4.01E-3	2.84E-2
090118	Swift	16	13.4	4 (15-150)	-0.30	0.56	4.49E-4	2.09E-3
090301A	Swift	41	14.1	230 (15-150)	-1.25	-1.50	4.46E-4	1.13E-3
090301315	Fermi	23.3	22.8	22.7 (10-1000)	0.56	1.20	1.41E-3	5.30E-3
090306B	Swift	20.4	38.5	31 (15-150)	1.24	0.11	1.14E-2	2.51E-2

* Corresponding author: zhouxx@swjtu.edu.cn (X. X. Zhou); chensz@ihep.ac.cn (S. Z. Chen)

090320801	Fermi	29.2	22.4	16.7 (10-1000)	-0.33	0.20	1.02E-3	3.97E-3
090328713	Fermi	0.2	15.5	1.19 (10-1000)	-0.60	-0.27	2.10E-5	1.06E-5
090403314	Fermi	14.8	29.7	10.9 (10-1000)	-0.04	-0.64	1.74E-3	3.97E-3
090425377	Fermi	75.4	44.2	181 (10-1000)	-0.22	0.31	1.79E-2	5.41E-2
090511684	Fermi	7.6	39.0	24.9 (10-1000)	0.34	-1.18	5.74E-3	7.84E-3
090520A	Swift	20	42.2	3.4 (15-150)	1.27	0.67	1.54E-2	3.60E-2
090529564	Fermi	9.9	22.1	86.9 (10-1000)	-0.86	-0.42	4.36E-4	1.77E-3
090617208	Fermi	0.2	16.1	9.43 (10-1000)	-0.51	-0.77	2.27E-5	8.00E-6
090621B	Swift	0.14	40.5	0.7 (15-150)	0.20	0.40	4.84E-4	2.34E-4
090704783	Fermi	19.5	4.3	15.8 (10-1000)	0.13	-1.30	4.50E-4	6.41E-4
090712	Swift	145	10.6	40 (15-150)	0.93	0.47	1.96E-3	5.60E-3
090730608	Fermi	9.1	4.4	31.8 (10-1000)	0.82	-0.03	4.01E-4	1.01E-3
090802235	Fermi	0.1	35.5	11.4 (10-1000)	0.07	0.43	2.21E-4	9.37E-5
090807A	Swift	140.8	19.9	22 (15-150)	1.21	2.42	3.37E-3	1.39E-2
090807832	Fermi	17.9	29.3	13.4 (10-1000)	-0.07	-0.44	1.74E-3	4.56E-3
090820027	Fermi	12.4	17.0	1540 (10-1000)	0.80	1.09	7.37E-4	2.56E-3
090831317	Fermi	39.4	35.7	94.4 (10-1000)	-1.61	-2.11	1.96E-3	1.87E-3
090904A	Swift	122	22.0	30 (15-150)	0.16	0.45	2.57E-3	8.81E-3
090904581	Fermi	38.4	32.9	16.4 (10-1000)	-0.64	0.52	3.04E-3	1.64E-2
091030828	Fermi	98.1	25.0	296 (10-1000)	0.08	0.36	2.49E-3	8.84E-3
091106762	Fermi	14.6	30.2	18.3 (10-1000)	1.53	0.44	3.10E-3	6.86E-3
091202	Integral	45	33.2	...	-1.96	-0.72	7.40E-4	1.03E-2
091215234	Fermi	4.4	25.5	9.87 (10-1000)	-0.89	0.29	3.83E-4	2.20E-3
091227294	Fermi	21.9	27.9	68.9 (10-1000)	-0.86	-0.40	1.09E-3	4.40E-3
100111A	Swift	12.9	21.5	6.7 (15-150)	0.22	-0.28	8.06E-4	2.00E-3
100115A	Swift	3	32.6	...	-0.85	0.19	7.57E-4	4.30E-3
100122616	Fermi	22.5	33.1	120 (10-1000)	-0.25	0.01	2.96E-3	1.06E-2
100131730	Fermi	3.5	14.1	73.4 (10-1000)	0.29	1.43	2.91E-4	1.39E-3
100210101	Fermi	29.2	24.9	21.1 (10-1000)	0.89	1.44	2.04E-3	7.31E-3
100225703	Fermi	4.5	8.5	16.1 (10-1000)	0.76	0.11	3.07E-4	8.19E-4

100513879	Fermi	11.1	38.7	37.1 (10-1000)	-1.57	-0.71	1.74E-3	1.26E-2
100522A	Swift	35.3	27.7	21 (15-150)	-0.30	-1.15	1.79E-3	3.17E-3
100525744	Fermi	1.5	13.7	6.44 (10-1000)	0.74	0.68	7.83E-5	3.10E-5
100526A	Swift	102	9.6	25 (15-150)	-0.33	-0.07	9.87E-4	3.70E-3
100527795	Fermi	184.6	33.3	139 (10-1000)	-1.93	-1.89	1.00E-2	3.13E-2
100614498	Fermi	172.3	43.2	196 (10-1000)	-0.16	-0.80	3.96E-2	7.36E-2
100625891	Fermi	29.2	15.4	14 (10-1000)	-0.43	-0.88	6.60E-4	1.50E-3
100713A	Integral	20	12.6	210 (20-200)	-0.56	-0.30	4.09E-4	1.53E-3
100714686	Fermi	5.6	39.9	15.6 (10-1000)	0.08	-0.24	4.84E-3	1.32E-2
100902A	Swift	428.8	37.1	32 (15-150)	1.08	0.75	3.99E-2	1.19E-1
101003244	Fermi	10	30.8	22.3 (10-1000)	1.71	0.51	2.91E-3	6.30E-3
101101744	Fermi	3.3	25.5	6.5 (10-1000)	0.07	-1.02	5.67E-4	9.41E-4
101107011	Fermi	375.8	25.8	72.6 (10-1000)	2.55	0.51	1.79E-2	3.59E-2
101112984	Fermi	82.9	39.8	85.7 (10-1000)	-0.71	-0.89	9.16E-3	2.56E-2
101123952	Fermi	103.9	28.2	1130 (10-1000)	1.49	0.99	6.39E-3	1.71E-2
101202154	Fermi	18.4	38.0	14.1 (10-1000)	-1.85	-1.58	1.26E-3	6.61E-3
101231067	Fermi	23.6	23.9	168 (10-1000)	0.32	-0.24	1.36E-3	3.24E-3
110106A	Swift	4.3	34.9	3 (15-150)	0.65	0.77	2.61E-3	9.01E-3
110210A	Swift	233	23.0	9.6 (15-150)	0.19	-0.16	3.87E-3	1.02E-2
110220761	Fermi	33	31.0	21.1 (10-1000)	-0.99	1.17	1.71E-3	1.41E-2
110226989	Fermi	14.1	36.9	19 (10-1000)	-1.16	-0.86	2.36E-3	9.74E-2
110312A	Swift	28.7	37.2	8.2 (15-150)	-0.002	0.84	6.91E-3	3.13E-2
110315A	Swift	77	19.4	41 (15-150)	0.26	0.96	1.73E-3	6.66E-3
110328520	Fermi	141.3	17.2	190 (10-1000)	-0.97	-0.96	1.27E-3	4.00E-3
110401920	Fermi	2.4	15.3	15.7 (10-1000)	-1.15	-1.00	1.13E-4	4.11E-4
110406A	Integral	8	31.1	...	0.85	0.35	2.13E-3	5.60E-2
110414A	Swift	152	44.2	35 (15-150)	-0.84	-0.69	1.93E-2	4.69E-2
110517573	Fermi	23	29.5	87.4 (10-1000)	-0.65	0.06	1.47E-2	6.50E-3
110605183	Fermi	82.7	33.8	193 (10-1000)	-1.30	-0.24	2.57E-3	1.80E-2
110625A	Swift	44.5	40.0	280 (15-150)	-1.07	-1.39	6.61E-3	1.53E-2

110626448	Fermi	6.4	40.4	11.6 (10-1000)	-0.003	-0.22	5.20E-3	1.47E-2
110629174	Fermi	61.7	5.1	24.3 (10-1000)	0.40	1.18	9.09E-4	3.96E-3
110705364	Fermi	19.2	18.7	89.4 (10-1000)	0.56	0.99	9.10E-4	3.30E-3
110706202	Fermi	12	26.9	32.7 (10-1000)	-0.22	-1.41	1.02E-3	1.34E-3
110706977	Fermi	33.2	29.3	65.5 (10-1000)	-1.41	-1.11	8.93E-4	3.82E-3
110709A	Swift	44.7	13.5	100 (15-150)	-0.35	-0.11	7.56E-4	2.73E-3
110709463	Fermi	24.1	26.7	69.1 (10-1000)	0.34	0.79	1.80E-3	6.47E-3
110820A	Swift	256	41.7	8.2 (15-150)	-0.07	0.16	3.31E-2	1.05E-1
110915A	Swift	78.76	39.5	57 (15-150)	0.42	-0.34	1.84E-2	4.20E-2
110919634	Fermi	35.07	42.6	268 (10-1000)	-0.63	-1.36	9.27E-3	1.43E-2
110921A	Swift	48	7.3	24 (15-150)	-0.30	-0.25	6.40E-4	2.21E-3
110928180	Fermi	148.2	8.5	142 (10-1000)	0.45	0.28	1.49E-3	4.69E-3
111017657	Fermi	11.1	40.0	207 (10-1000)	1.78	2.28	1.16E-2	4.17E-2
111024A	MAXI	0.2	10.7	...	-0.20	-0.30	2.06E-5	8.33E-6
111103B	Swift	167	41.6	80 (15-150)	0.23	-0.22	3.06E-2	4.04E-2
111109873	Fermi	9.7	32.1	66.9 (10-1000)	-0.26	0.81	1.66E-3	8.16E-3
111117A	Swift	0.47	38.5	1.4 (15-150)	2.18	1.80	1.12E-3	3.66E-4
111127810	Fermi	19	30.2	86.4 (10-1000)	0.81	-1.63	2.74E-3	1.83E-3
111208A	Swift	20	11.1	9.8 (15-150)	-1.54	-0.12	1.70E-4	1.59E-3
111215A	Swift	796	30.6	45 (15-150)	-3.51	-1.21	1.35E-2	2.04E-2
111228453	Fermi	2.9	23.9	27.5 (10-1000)	0.479	1.68	5.37E-4	2.44E-3
120102A	Swift	38.7	44.8	43 (15-150)	-1.80	-1.36	3.14E-3	1.34E-2
120106A	Swift	61.6	35.4	9.7 (15-150)	-0.27	0.26	6.76E-3	2.77E-2
120118898	Fermi	17.2	18.2	16.2 (10-1000)	-0.75	-1.26	4.53E-4	9.46E-4
120129A	IPN	4	38.5	...	-0.44	-0.01	2.71E-3	1.12E-2
120202A	Integral	100	15.6	0.7 (20-200)	-0.98	0.38	8.43E-4	5.17E-3
120217808	Fermi	5.9	38.8	17.5 (10-1000)	-0.74	1.01	2.77E-3	1.96E-2
120219A	Swift	90.5	32.1	5.4 (15-150)	-1.09	-1.25	3.16E-3	8.56E-3
120222021	Fermi	1.1	44.1	17.3 (10-1000)	2.39	1.72	1.74E-3	6.81E-4
120223933	Fermi	14.3	37.6	38.8 (10-1000)	0.46	0.003	6.28E-3	1.71E-2

120226447	Fermi	14.6	36.9	58.5 (10-1000)	-0.003	-1.51	4.83E-3	5.44E-3
120512A	Integral	40	36.8	...	-2.52	-0.34	6.90E-3	2.10E-2
120519721	IPN	0.96	43.8	24.1 (15-150)	0.06	-0.05	7.83E-4	3.48E-4
120522361	Fermi	28.2	40.2	93.2 (10-1000)	0.17	-0.59	1.10E-2	2.37E-2
120612680	Fermi	63.2	21.5	20.6 (10-1000)	-0.31	-0.70	1.47E-3	3.71E-3
120625119	Fermi	7.4	21.2	102 (10-1000)	-0.89	0.21	3.37E-4	1.87E-3
120703498	Fermi	77.6	21.8	26 (10-1000)	0.49	0.47	2.29E-3	6.97E-3
120819A	Swift	71	42.3	14 (15-150)	0.29	0.91	2.00E-2	6.87E-2
120905657	Fermi	195.6	41.9	195.7 (10-1000)	-0.30	-0.15	2.67E-2	8.16E-2
120915474	Fermi	5.9	40.9	3.8 (10-1000)	0.08	-0.57	5.47E-3	1.20E-2
121011A	Swift	75.6	19.3	27 (15-150)	1.10	0.38	2.29E-3	5.66E-3
121012724	Fermi	0.45	24.5	12.7 (10-1000)	0.19	0.57	7.83E-5	3.26E-5
121025A	MAXI	20	6.9	...	-0.42	-0.72	3.61E-4	1.04E-3
121108A	Swift	89	36.2	9.6 (15-150)	0.19	-0.10	1.18E-2	3.24E-2
121113544	Fermi	95.5	34.5	268.5 (10-1000)	-0.32	-1.07	7.43E-3	1.39E-2
121123A	Swift	317	42.1	150 (15-150)	0.25	0.60	4.38E-2	1.38E-1
121202A	Swift	20.1	27.2	12 (15-150)	0.99	1.81	2.10E-3	8.04E-3
121211695	Fermi	9.0	23.7	13.4 (10-1000)	0.31	0.83	8.39E-4	3.11E-3
130122A	Swift	64	30.6	7.4 (15-150)	0.48	-0.53	4.85E-3	8.94E-3

Notes. Column 1: GRB name (GCN name for Swift GRBs and Trigger ID for Fermi GRBs). Column 2: satellite that detected the GRB. Column 3: burst duration T_{90} as measured by the respective satellite. Column 4: zenith angle at the ARGO-YBJ location. Column 5: fluence in the keV range measured by the satellite that detected the burst. Column 6 and 7: statistical significance of the ARGO-YBJ cluster detected during the prompt phase, for two values of E_{cut} (100 GeV and 1 TeV). Column 8 and 9: 99% C. L. upper limits to the fluence for two values of E_{cut} (100 GeV and 1 TeV).

Table 3

List of 24 GRBs with known redshift occurred in the field of view of ARGO-YBJ

GRB (1)	Satellite (2)	α_{SAT} (3)	z_{SAT} (4)	T_{90} (s) (5)	θ ($^{\circ}$) (6)	keV fluence (10^{-7} erg cm $^{-2}$) (keV range) (7)	σ_1 (10-100 GeV) (8)	σ_2 (10-1000 GeV) (9)	F_{UL1} (erg cm $^{-2}$) (10-100 GeV) (10)	F_{UL2} (erg cm $^{-2}$) (10-1000 GeV) (11)
071112C	Swift	1.09	0.82	15	18.42	30 (15-150)	0.25	0.12	8.90E-4	4.70E-4
080207	Swift	1.58	2.09	340	27.7	61 (15-150)	-0.24	0.15	7.29E-3	2.78E-2
080602	Swift	1.43	1.82	74	41.9	32 (15-150)	0.63	1.63	1.94E-2	6.48E-2
081028A	Swift	1.25	3.04	260	29.9	37 (15-150)	2.43	0.81	2.90E-2	1.14E-1
081128	Swift	1.98	<4	100	31.8	23 (15-150)	0.05	-0.80	1.64E-2	1.11E-1
090407	Swift	1.73	1.45	310	45	11 (15-150)	-0.78	0.16	1.58E-2	3.86E-2
090417B	Swift	1.85	0.35	260	37.2	23 (15-150)	-0.52	0.12	5.91E-3	9.93E-4
090424	Swift	1.19	0.54	48	33.1	210 (15-150)	-0.15	-0.06	1.56E-3	4.47E-4
090529A	Swift	2.00	2.63	100	19.9	6.8 (15-150)	-0.76	0.12	2.09E-3	1.53E-2
090902B	Fermi	1.94	1.82	19.3	23.3	4058 (10keV-10GeV)	-0.89	-1.02	5.32E-4	1.34E-3
100206A	Swift	0.63	0.41	0.12	26.8	1.4 (15-150)	-0.71	0.85	3.80E-5	2.49E-5
100418A	Swift	2.16	0.62	7	18.7	3.4 (15-150)	-0.72	-0.59	1.07E-4	2.55E-5
100424A	Swift	1.83	2.47	104	33.4	15 (15-150)	1.43	1.70	1.71E-2	8.40E-2
100728A	Swift	1.18	1.57	198.5	44.9	380 (15-150)	0.55	0.19	2.51E-2	3.58E-2
101224A	Swift	1.05	0.72	0.2	22.6	0.58 (15-150)	-0.10	-0.42	4.70E-5	2.16E-5
110106B	Swift	1.76	0.62	24.8	25.1	20 (15-150)	-1.40	-0.83	1.80E-4	1.22E-4
110128A	Swift	1.31	2.34	30.7	43.2	7.2 (15-150)	-0.06	0.16	1.63E-2	5.66E-2
111211A	AGILE	2.77	0.48	15	20.3	92 (20-1200)	0.16	0.16	2.45E-4	6.41E-5
120118B	Swift	2.08	2.94	23.2	42.7	18 (15-150)	-0.71	-0.45	1.53E-2	7.77E-2
120326A	Swift	2.06	1.8	69.6	41.0	26 (15-150)	-0.24	0.25	1.22E-2	3.80E-2

120716A	IPN	CPL	2.49	230	35.7	147 (10-1000)	-1.39	-1.32	9.01E-3	4.61E-2
120722A	Swift	1.90	0.96	42.4	17.7	12 (15-150)	-0.18	-0.80	4.20E-4	2.36E-4
120907A	Swift	1.73	0.97	16.9	40.2	6.7 (15-150)	0.10	0.38	3.46E-3	3.34E-3
130131B	Swift	1.15	2.54	4.3	27.3	3.4 (15-150)	0.80	0.19	1.45E-3	5.91E-3

Notes. Column 1: GRB name (GCN name for Swift GRBs and Trigger ID for Fermi GRBs). Column 2: satellite that detected the burst. Column 3: spectral index reported by the satellite: “CPL” means that the spectrum measured by the satellite is fitted with a cutoff power law. Others are fitted by a simple power law. Column 4: redshift. Column 5: burst duration T_{90} as measured by the respective satellite. Column 6: zenith angle at the ARGO-YBJ location. Column 7: fluence in the keV range measured by the satellite that detected the burst. Column 8 and 9: statistical significance of the cluster detected during the prompt phase, for two E_{cut} values (100 GeV and 1 TeV). Column 10 and 11: 99% C. L. upper limits to the fluence for two E_{cut} values (100 GeV and 1 TeV) with $\alpha = 2.0$ ($\alpha = 1.94$ for GRB 090902B).